In Situ Orthorhombic to Amorphous Phase Transition of Nb_2O_5 and Its Temperature Effect on Pseudocapacitive Behavior

Shaoning Zhang, Jinkwang Hwang,[*] Kazuhiko Matsumoto,[*] Rika Hagiwara

Graduate School of Energy Science, Kyoto University, Yoshida-honmachi, Sakyo-ku, Kyoto 606-8501, Japan

*Corresponding Author

E-mail: k-matsumoto@energy.kyoto-u.ac.jp (K.M.) and hwang.jinkwang.5c@kyoto-u.ac.jp (J.H)

ABSTRACT

Niobium pentoxide (Nb_2O_5) represents an exquisite class of negative electrode materials with unique pseudocapacitive kinetics that engender superior power and energy densities for advanced electrical energy storage devices. Practical energy devices are expected to maintain stable performance under real-world conditions such as temperature fluctuations. However, the intercalation pseudocapacitive behavior of Nb_2O_5 at elevated temperatures remains unexplored due to the scarcity of suitable electrolytes. Thus, in this study, we investigate the effect of temperature on the pseudocapacitive behavior of submicron-sized Nb_2O_5 in a wide potential window of 0.01–2.3 V. Furthermore, ex-*situ* X-ray diffraction and X-ray photoelectron measurements reveal the amorphization of Nb_2O_5 accompanied by the formation of NbO via a conversion reaction during the initial cycle. Subsequent cycles yield enhanced performance attributed to a series of reversible $Nb^{V, IV}/Nb^{III}$ redox reactions in the amorphous $Li_xNb_2O_5$ phase. Through cyclic voltammetry and symmetric cell electrochemical impedance spectroscopy, temperature elevation is noted to increase the pseudocapacitive contribution of the Nb_2O_5 electrode resulting in high-rate capability of 131 mAh g^{-1} at 20000 mA g^{-1} at 90 °C. The electrode further exhibits long-term cycling over 2000 cycles and high Coulombic efficiency ascribed to the formation of robust, $[FSA]^-$ originated solid-electrolyte interphase during cycles.

Keywords: pseudocapacitive materials, niobium oxides, lithium storage mechanism rate capabilities; ionic liquids; amorphization

INTRODUCTION

Energy storage devices have been acclaimed to be the driving force behind the global electro-mobility revolution, exemplifying the yardstick for emergent transport technologies. At the peak of the vibrant rechargeable battery market, lithium-ion batteries (LIBs) have become ubiquitous in a wide swath of applications owing to their remarkable power and energy densities.[1-3] Despite this success, the viability of secondary batteries for modern energy storage applications have been called into question, as growing demands for higher charge-discharge rate capabilities, superior energy and power densities, and improved safety continue to encroach on LIB theoretical limits. Thus, the advancement of LIB technologies and pertinent components is of paramount importance to future mobility systems and energy applications.

Against this backdrop, it is evident that current commercialized LIBs, which mostly employ graphite-based negative electrode materials, cannot fulfil future energy needs due to their limited ion kinetics and resultant inferior rate capabilities.[4-7] As a solution, silicon-based compounds have been proposed as possible replacements on the grounds of their high Li-ion storage capacities. However, electrodes derived from these materials have been found to undergo large volume changes during (de)lithiation processes, causing cell degradation and safety concerns during cycling.[8-10] These issues have led to the exploration of the $Li_4Ti_5O_{12}$ (LTO) electrode as a candidate for commercialization, for it exhibits not only minimal volume changes during the charge-discharge processes but also displays excellent rate performance.[11] Even so, the practical utility of this insertion-type negative electrode is heavily hampered by its low capacities as well as complications related to gas evolutions during elevated temperature operations.[12]

In the search for high-performance negative electrodes, niobium pentoxide (Nb_2O_5) has emerged as a providential contender on account of its structural expedience, agile Li^+ diffusion,

high theoretical capacity (201.7 mAh g^{-1} based on Nb^{5+}/Nb^{4+}), and relatively low working potential (1.0−1.5 V vs. Li^+/Li).[13, 14] Additionally, Nb_2O_5 exhibits a rich crystal versatility which allows the synthesis of several polymorphs; pseudohexagonal, orthorhombic, tetragonal, monoclinic and amorphous Nb_2O_5 under different conditions. Previous reports on this material have shown the crystal structure and the crystallinity of Nb_2O_5 to have immense influence on their emergent electrochemical behavior.[15-17] In a study on the electrochemical properties of micrometre-sized Nb_2O_5 polymorphs by Griffith *et al.*, tetragonal Nb_2O_5 was found to deliver the lowest charge-discharge performance among the polymorphs. The monoclinic Nb_2O_5 showed the highest reversible capacity but exhibited inferior rate capability (approximately 140 mAh g^{-1} at 2000 mA g^{-1}) compared to the pseudohexagonal Nb_2O_5 and the orthorhombic Nb_2O_5 crystal structures.[18] Although most polymorphs in this family display exemplary electrochemical behavior, the orthorhombic Nb_2O_5 has shown the most auspicious prospects as a negative electrode material, with ultrafast Li storage and unique capabilities derived from the so-called 'intercalation pseudocapacitance.[19, 20]

Pseudocapacitance entails reversible faradaic charge storage mechanisms involving rapid redox reactions at the surface or near-surface regions of an electrode, resulting in high energy densities and excellent charge-discharge rates. These mechanisms allow the pseudocapacitive materials to transcend the capacity constraints of electrical double-layer capacitor (EDLC) materials while exceeding the mass transfer limitations of the typical battery electrodes, delivering high levels of charge storage within short periods of time (10 seconds–10 minutes).[21] Interest in these materials has been exacerbated by the recent progress in the cognizance of nanomaterials that have proffered new synthetic routes for advanced pseudocapacitive materials such as RuO_2, V_2O_5, MnO_2, MoS_2, Nb_2O_5 and TiO_2. These materials, which embody nanostructures such as

nanoporous structures,[22-24] nanosheets,[25] nanobelts,[26] nanotubes,[27] nanocrystals,[28, 29] and nanocomposites[30] display enhanced pseudocapacitive behavior attributed to the significantly reduced diffusion distances and the large surface areas of their small nanosized particles. In spite of these merits, the large surface areas in nanostructures have been found to cause increased electrode dissolution, low packing density, enhanced electrolyte decomposition, and recurrent synthetic complexities, indeed detrimental effects to battery performance.[31, 32] Therefore; research efforts have shifted towards the use of larger micrometre-sized particles as a strategy to achieve a rapid pseudocapacitive response (thereby, high energy and power densities) for practical applications.

It is worth noting that attempts to 'future-proof' LIBs for next-generation energy demands have galvanised research efforts into numerous aspects besides negative electrode performance. For instance, the ability to sustain stable operations at intermediate temperatures (above room temperatures) and tolerance to spontaneous temperature fluctuations without compromising safety is expected to become key requisites for future battery applications.[33] However, contemporary commercialized LIBs, which generally utilise carbonate-based organic electrolytes, are known to be unsuitable for elevated temperatures operation due to diminished performance caused by electrolyte degradation and potential fire hazards.[34-36] These safety concerns have generated traction among ionic liquid (IL) electrolytes which have been deemed to have high resilience to temperature elevations and fluctuations attributed to their non-flammability and low volatility.[33, 37, 38] Furthermore, intermediate-temperature operations have been found to ameliorate the performance of IL electrolytes, thus creating a new avenue for utilizing the ubiquitous waste heat in daily activities.[33, 39, 40]

It is evident that pseudocapacitive materials, particularly Nb_2O_5, represent an exquisite

class of energy materials that promise to revolutionise battery capabilities beyond the contemporary scopes of battery performance. However, studies on the Nb_2O_5 negative electrode, which typically entail analyses on half-cell configurations in the 1.0–3.0 V cutoff voltage range, are yet to provide a full picture into the electrochemical capabilities of this material. Thus, to shed light on their performance in wider voltage ranges, recent inquests have revealed the Nb_2O_5 electrode to have excellent cycle stability and rate capability in the extended range of 0.0-3.0 V.[41-44] Even so, the pertinent charge storage mechanisms in the wider voltage ranges and the effect of external factors such as temperature, especially in LIB systems, are still not well understood.[45] Therefore, in a bid to gain comprehensive insights into the effect of temperature on the pseudocapacitive behavior and charge-discharge mechanisms of the Nb_2O_5 pseudocapacitive material, this study reports the influence of temperature on the electrochemical properties of a non-modified (commercial powder) orthorhombic Nb_2O_5 negative electrode in the cutoff voltage range of 0.01–2.3 V vs. Li^+/Li with the aid of a thermally stable Li[FSA]-[C_2C_1im][FSA] ($[FSA]^-$ = bis(fluorosulfonyl)amide and $[C_2C_1im]^+$ = 1-ethyl-3-methylimidazolium) IL electrolyte at 25 and 90 °C. *Ex-situ* XRD (X-ray diffraction) and X-ray photoelectron spectroscopic (XPS) analyses are employed to investigate the structural evolution of the electrode during the charge-discharge processes. The capacitive contribution to Li storage processes of the electrode is further evaluated using cyclic voltammetry (CV) tests and symmetric cell electrochemical impedance spectroscopy (SCEIS).

EXPERIMENTAL SECTION

Materials and Handling. All samples used in this study were handled under a dry Ar atmosphere in a glove box (H_2O < 1 ppm and O_2 <1 ppm). Nb_2O_5 (Wako Pure Chemical Industries, purity:

99.9%) was used as-purchased to prepare electrode materials. The Li[FSA] (Mitsubishi Materials Electronic Chemicals, purity > 99%) and [C_2C_1im][FSA] (Kanto Chemical, purity > 99.9%; water content < 20 ppm) salts were dried under vacuum for 24 h at 80 °C prior to use.

Cell Preparation. The Li[FSA]-[C_2C_1im][FSA] IL electrolyte was prepared by mixing Li[FSA] and [C_2C_1im][FSA] in the 20:80 mol% (1.1 mol dm^{-3}).[46] Water content of the prepared Li[FSA]-[C_2C_1im][FSA] IL was kept below 20 ppm according to Karl-Fischer titration (899 Coulometer, Metrohm). A glass microfiber filter (Whatman GF/A) immersed in the IL electrolyte was used as a separator.

A slurry was prepared by well-mixing the commercial Nb_2O_5 with Super C65 (Timcal Ltd.) and PAI (Polyamide-imide) binder in the 70:20:10 wt% with NMP (*N*-methylpyrrolidone) using a planetary mixer (AR-100, Thinky, Tokyo, Japan). The resulting slurry was pasted on a Cu foil and dried under vacuum at 120 °C for 12 h. Electrode discs, 10 mm in diameter, were punched out of the foil. The loading mass of the electrode was approximately 0.7 mg cm^{-2}. Type-2032 coin cells (Li/IL/Nb_2O_5) were assembled using the prepared IL electrolyte, Nb_2O_5 electrode, and lithium metal counter electrode (Sigma-Aldrich Chemistry, 99.95% purity) fixed on a stainless steel (SUS316L) plate.

Material characterization. XRD patterns were collected under the Bragg-Brentano geometry using a Rigaku SmartLab diffractometer with Ni-filtered Cu-*K*α radiation (40 kV and 30 mA) and a silicon strip high-speed detector (Rigaku D/teX Ultra 250). The crystal structures were visualized using the VESTA program.[47] The morphology of the active material was investigated through scanning electron microscopy (SEM) (Hitachi SU-8020). The Brunauer-Emmett-Teller (BET)

method based on nitrogen adsorption analysis was employed to evaluate the surface area of electrode materials using a Tristar II 3020 equipment (Shimadzu Corp.). The oxidation state and solid-electrolyte interphase (SEI) layer components of the Nb_2O_5 electrodes were analysed by XPS (JEOL, JPS-9030, Mg *K*α source). All *ex-situ* samples for XRD and XPS after electrochemical tests were washed with THF (tetrahydrofuran) and dried under vacuum at room temperature.

Electrochemical Measurements. The electrochemical data were controlled by an HJ-SD8 charge-discharge system (Hokuto Denko) at 25 and 90 °C. A current density of 200 mA g^{-1} was applied to observe basic charge-discharge behavior. Discharge rate performance was performed under discharge current rates ranging from 200 mA g^{-1} to 20000 mA g^{-1} and constant charge current rate of 200 mA g^{-1}. CV was performed at a scan rate from 0.5 to 50 mV s^{-1} controlled by a VSP potentiostat (Bio-Logic) at 25 and 90 °C.

The SCEIS analysis was conducted on the identical electrodes from the half-cell setup after adjusting their voltage. The cells were first fully charged to 0.01 V and discharged to 1.0 V. Symmetric cells (Nb_2O_5/IL/Nb_2O_5) were assembled under a dry Ar atmosphere. EIS data were obtained by a VSP potentiostat (Bio-Logic) at 25, 70 and 90 °C in a frequency range from 0.1 Hz to 100 kHz. All the electrochemical measurements were performed with the relevant temperature adjustment of at least 2 h.

RESULT AND DISCUSSION

Characterization of Nb_2O_5 electrode. Previous studies on secondary batteries utilising IL electrolytes have shown that temperature elevation activates room-temperature inert materials, thereby enhancing ion diffusion in both the electrolyte and the electrode and improving their

interfacial processes.[48] As shown by the schematic in **Figure 1a**, the contribution of pseudocapacitive mechanisms in the Li storage of Nb_2O_5 is expected to increase at higher temperatures, given the beneficial effects of temperature on the ionic conductivity and viscosity of the Li[FSA]-[C_2C_1im][FSA] IL electrolyte. The plot showing the correlation between the IL electrolyte temperature, ionic conductivity and viscosity in **Figure 1b** has been derived from a previous study.[46] Consequently, the Nb_2O_5 electrode is posited to display highly enhanced pseudocapacitive energy storage when used alongside the IL electrolyte at elevated temperatures. As such, understanding the effect of temperature on the pseudocapacitive behavior of Nb_2O_5 is vital for its future exploitation.

In this study, submicron-sized (or non-fabricated) Nb_2O_5 with an average diameter of approximately 300 nm (see **Figure S1**) was selected. XRD analysis on the present Nb_2O_5 indicated the crystal lattice belongs to the orthorhombic space group *Pbam* as shown in **Figure S2**. The surface areas of the composite electrode material, Nb_2O_5-Super C65 and its constituent materials: pristine Nb_2O_5 and Super C65, were obtained as shown in **Figure S3**. The non-fabricated Nb_2O_5 was found to have a surface area of 5.5 $m^2 g^{-1}$: one order of magnitude smaller than Nb_2O_5 nano-architectures such as the *T*-Nb_2O_5 nanoparticle (59.0 $m^2 g^{-1}$),[28] the *TT*-Nb_2O_5 (57.5 $m^2 g^{-1}$), [49] and the Nb_2O_5 nanoparticle (57.5 $m^2 g^{-1}$);[50] three orders of magnitude smaller than the surface area of the conventional activated carbon (approximate 2000 $m^2 g^{-1}$).[51]

Investigation on the charge-discharge mechanism and amorphization. The storage mechanism of Nb_2O_5 electrode in the IL electrolyte at 25 and 90 °C were investigated through XPS and *ex-situ* XRD measurements performed on pristine electrodes and electrodes at different SOC of the initial cycle with different cutoff voltages, respectively, as reflected in the charge-discharge profiles in Figure 2a,c. The XRD patterns are labelled as Patterns a-i alongside their corresponding

XPS spectra denoted as Spectra a-e, h, and i. Considering that ion-beam bombardment has been known to cause the reduction of metal oxides (in this case Nb_2O_5), the lowest Ar beam intensity was used for the present XPS analyses.[52] Before the initial charge-discharge process (a→b→c) at 25 °C, the pristine electrode (Spectrum a) shows an Nb $3d_{5/2}$ peak at 206.9 eV ascribed to the constituent Nb in the orthorhombic Nb_2O_5.[53] After the initial charge to 1.0 V (lithiation), two peaks: $3d_{5/2}$ and $3d_{3/2}$ are noted to appear at 205.7 and 208.5 eV, respectively (Spectrum b), signifying that Nb^V was reduced to Nb^{IV}.[54] When the electrode was discharged from 1.0 to 2.3 V (delithiation), the XPS peaks (Spectrum c) were observed to recover back to their original positions in the pristine state—evidence that the Nb^V/Nb^{IV} redox reaction is reversible. The reversibility of the charge-discharge process in the 1.0–2.3 V cutoff voltage range is further affirmed by the *ex-situ* XRD patterns (Patterns a-c). The XRD peaks in the pristine state (Pattern a) confirm orthorhombic Nb_2O_5 with diffraction peaks at 2θ = 22.61° (001 line), 28.40° (180 line), and 36.60° (181 line). The XRD peaks shift to lower angles upon lithiation to 1.0 V (Pattern b) and reverting to their original positions in the pristine state after delithiation to 2.3 V (Pattern c). These reversible peaks shift clearly demonstrates that the crystalline framework of orthorhombic Nb_2O_5 is preserved during the charge-discharge in cutoff voltage range of 1.0–2.3 V.[55]

Subsequently, the electrode was subjected to a charge-discharge process in the extended cutoff voltage range of 0.01–2.3 V (a→d→e). When the Nb_2O_5 electrode is charged to 0.01 V (Spectrum d), $3d_{5/2}$ peaks assigned to the Nb^{III} and Nb^{II} oxidation states appear in the 203–205 eV range.[56] At this SOC, the pertinent XRD peaks (Pattern d) are observed to shift to lower angles, suggesting that the orthorhombic Nb_2O_5 is further lithiated during the extended charge.[57] Thereafter, the XPS peaks (Spectrum e) virtually return to their original positions when the electrode is discharged from 0.01 to 2.3 V, evincing to the reversibility of the $Nb^V/Nb^{IV}/Nb^{III}$

reaction. The mechanisms involved in this (1st) cycle are elaborated by XRD Pattern e, which suggests the occurrence of a phase transition from the orthorhombic Nb_2O_5 to an amorphous (a-$Li_xNb_2O_5$) phase. The XRD pattern obtained during this cycle further reveals that NbO was formed via a conversion reaction during the first charge to 0.01 V (Pattern d) and was retained even after discharge to 2.3 V (Pattern e), signifying that the NbO formed was not involved in the charge-discharge reaction. These results are corroborated by the presence of a Nb $3d_{5/2}$ XPS peak at 203.8 eV in Spectrum e, attesting to the presence of NbO in the discharged state.

Similar observations were made when the Nb_2O_5 electrodes at the different SOCs were subjected to XPS and XRD analyses at 90 °C, implying that the charge-discharge mechanisms involved amorphization and the formation of NbO via a conversion reaction during the initial charge to 0.01 V. The XRD patterns obtained at both temperatures confirm that the NbO formed after the extended charge to 0.01 V (Patterns d and h) exists in a cubic phase with diffraction peaks at $2\theta = 29.99°$ (110 line) and 36.95° (111 line).[58] Despite these similarities, the corresponding XPS spectra revealed some distinctions in the Li storage mechanisms of the Nb_2O_5 at the different temperatures. Here, the intensities of the Nb^{IV}, Nb^{III}, and Nb^{II} XPS peaks were found to be stronger at 90 °C (Spectrum h) than at 25 °C (Spectrum d), signifying that the higher capacities (effectively higher Li storage) obtained during the extended charge-discharge at 90 °C results from the involvement of larger amounts of activated Nb_2O_5 in the redox reaction which is accompanied by higher production of NbO.

For a full picture of the mechanisms involved during the charge and discharge of the Nb_2O_5 electrode, a schematic summary is provided in **Figure 2d**. As shown in the illustration, Li storage during operations in the 1.0–2.3 V cutoff voltage range occured through a reversible Nb^V/Nb^{IV} redox reaction in the orthorhombic Nb_2O_5 phase. However, when charging was extended to 0.01

V, a phase transition from the orthorhombic $Li_xNb_2O_5$ to the a-$Li_xNb_2O_5$ amorphous phase occurred, which was accompanied by a partial conversion reaction to NbO and Li_2O (see XRD pattern in **Figure S4**). Subsequent lithiation-delithiation processes in the 0.01–2.3 V cutoff voltage range were noted to occur exclusively in the a-$Li_xNb_2O_5$ amorphous phase via a reversible $Nb^{V,IV}/Nb^{III}$ reaction, while the diffraction peaks of the NbO phase remained unchanged in the subsequent cycles, as shown in the XRD pattern obtained after 300 cycles (**Figure S4**). It is worth noting that improvements in the electrochemical performance in other metal oxide negative electrode materials such as amorphous V_2O_5 [59] and amorphous $Li_4Ti_5O_{12}$,[60] have previously been accredited to the high Li-ion diffusion engendered by the enhanced diffusion pathways in their amorphous phases. The amorphization of Nb_2O_5 observed in the study can be expected to have a contribution to the agile (de)lithiation processes and result in the high-rate capabilities of a-$Li_xNb_2O_5$ within the extended cutoff voltage.

Electrochemical performance of a-$Li_xNb_2O_5$. The electrochemical performance of the Nb_2O_5 electrode at (a) 25 and (b) 90 °C was examined through galvanostatic charge-discharge tests performed on Li/IL/Nb_2O_5 half cells at a current density of 200 mA g^{-1} as shown in **Figure 3a,b**. The initial charge process conducted at 25 °C delivered a large irreversible capacity of 520 mAh g^{-1}, consistent with the occurrence of electrolyte decomposition during the SEI formation (**Figure 3a**). Subsequent cycling thereafter achieved relatively lower capacities (210.0 mAh g^{-1} at the 5th cycle) characterised by virtually overlapping profiles, demonstrating the reversible electrochemical behavior of the electrode at room temperature. During operations at 90 °C, the initial charge yielded a capacity of 1220 mAh g^{-1} (**Figure 3b**) evincing that the formation of the SEI layer involved intensified electrolyte decomposition at elevated temperatures. A detailed

interpretation of the SEI components is furnished later in this section. Further, the subsequent charge-discharge profiles obtained at 90 °C exhibited higher discharge capacities (408.9 mAh g^{-1} at the 5th cycle) than those at 25 °C: affirming that temperature elevation improved the performance of Nb_2O_5 electrode in the IL electrolyte. For deeper insight into the improved performance at intermediate temperatures, the rate capabilities of Li/IL/Nb_2O_5 half cells at 25 and 90 °C were evaluated under the current densities of 200 mA g^{-1} during charging and 200–20000 mA g^{-1} during discharge (**Figure 3c** and **Table S1**). Discharge curves obtained from both temperature operations indicate the polarization increased when higher current densities were applied (**Figure S5**). Notably, humps appearing around 1.5 V divide the discharge curves into two voltage regions with distinct polarization trends. Here, polarization in the lower potential region (0.01–1.5 V) was seen to be less than that of the higher potential region (1.5–2.3 V), suggesting the occurrence of different electrochemical processes in the two regions. Nonetheless, the electrode manifested high-rate capabilities across the different current densities, delivering discharge capacities of 119.8 mAh g^{-1} at 4000 mA g^{-1}, 98.5 mAh g^{-1} at 10000 mA g^{-1} and 86.0 mAh g^{-1} at 20000 mA g^{-1} during operations at 25 °C (**Figure 3c**). On the other hand, discharge curves obtained at 90 °C not only exhibit lower polarization than their room temperature equivalents but also display even higher rate capabilities marked by larger discharge capacities of 234.8 mAh g^{-1} at 4000 mA g^{-1}, 183.0 mAh g^{-1} at 10000 mA g^{-1} and 130.6 mAh g^{-1} at 20000 mA g^{-1}.

To determine the influence of intermediate temperatures on the long-term performance of the Nb_2O_5 electrode, the Li/IL/Nb_2O_5 half cells were cycled for 2000 cycles at 25 and 90 °C at 2000 mA g^{-1}. Prior to the cycle evaluation, the cells were subjected to an ageing process involving 5 cycles at 400 mA g^{-1} and 5 cycles at 1000 mA g^{-1}. As shown in **Figure 3d**, the cell achieved a

stable cycle performance during cycling at 25 °C, delivering a reversible capacity of 89.2 mAh g^{-1} in the initial cycle and capacity retentions of 102.6, 94.5 and 96.1% at the 100th, 1000th, and 2000th cycles, respectively (**Table S2**). On the other hand, cycling at 90 °C attained a higher reversible capacity of 279.2 mAh g^{-1} after the initial cycle, whereafter a gradual capacity fade was observed, culminating in a discharge capacity of 167.4 mAh g^{-1} at the 2000th cycle (see **Figure S6** for charge-discharge profiles). Although degradation is observed in the first few cycles, the Li/IL/Nb_2O_5 cells showed excellent tolerance to intermediate temperatures with a minimal capacity fade and a high average Coulombic efficiency (99.4%) over the 2000 cycles. Overall, the Nb_2O_5 electrode manifested enhanced performance denoted by fast and stable Li storage capabilities within a-$Li_xNb_2O_5$ at elevated temperatures which result from the deeper redox reactions contributing to the effectively higher Li storage. Comparatively, attention should be also paid to the inferiority in high-rate tolerance and instability of the performance especially at 90 °C with narrowed cutoff voltage of 1.0–2.3 V (see **Figures S7**, **S8**, and **S9** for charge-discharge profiles, rate capability, and cycle performance, respectively). The results lead to the conclusion that the enhanced electrochemical performance at wider cutoff voltage is benefitted from the amorphization progress due to the first charge to 0.01 V followed by the deeper redox reaction in a-$Li_xNb_2O_5$. Formation of the NbO phase with high electronic conductivity as described above may also contribute to the stable charge-discharge behavior. For a long time, the intrinsic pseudocapacitive behavior of Nb_2O_5 has been thought to be highly dependent on its crystalline structure.[15] However, the current study clearly demonstrates that a-$Li_xNb_2O_5$ can also exhibit rapid pseudocapacitive responses, especially at elevated temperatures.

Kinetic analysis of a-$Li_xNb_2O_5$. As earlier envisioned by the discharge curves in the rate capability tests (**Figure S5**), Li storage in the Nb_2O_5 involves two different electrochemical

processes. Therefore, to ascertain the exact nature of the charge-discharge mechanisms at different temperatures, Li/IL/Nb_2O_5 half cells at 25 and 90 °C were subjected to CV at scan rates varying from 0.5 to 50 mV s^{-1}. The charge-discharge processes in pseudocapacitive materials (in this case, Nb_2O_5) typically encompasses two distinctive mechanisms, *i.e.*, diffusion-controlled and capacitive-controlled processes. The contribution of the capacitive process in the overall Li storage is determined through the so-called *b*-value analysis, which involves investigating the correlation between the scan rate (v) and observed current (i), in accordance with Equation 1 and 2: [61]

$$i = av^b \quad (1)$$

$$\log(i) = b\log(v) + \log a \quad (2)$$

Here, a and b are adjustable parameters. Parameter b is represented by the slope of the log(i) vs. log(v) plot. Here, b = 0.5 corresponds to the diffusion-controlled process while b = 1.0 denotes the capacitive processes. This analysis is also used to evaluate the capacitive process and the diffusion-controlled process in the targeted sample.[61] **Figure 4a,c** show the CV curves obtained from the Nb_2O_5 electrode at 25 and 90 °C under different scan rates. The CV curves are characterized by two cathodic and anodic peaks that appear across the potential range at both temperatures. During this kinetic analysis, the current density was also noted to increase across all potential regions when the measurement temperature was increased, becoming prominent at high potentials. Further, the corresponding log(i) *vs.* log(v) plots were derived from the anodic and cathodic peaks obtained during both temperature operations (**Figure 4b,d**) by applying Equation 2. Here, the *b*-values of all redox peaks obtained at 90 °C were observed to be relatively higher than those obtained at 25 °C, suggesting that capacitive behavior was more dominant at the elevated temperature. The *b*-values were also found to be higher in low potential regions

(anodic/cathodic 1 and 3) than those in the high potential regions (anodic/cathodic 2 and 4) during both temperature operations. These results indicate that the high potential region is more diffusion-controlled, whereas the low potential region is more capacitive-controlled. Nevertheless, the capacitive mechanisms appear to dominantly influence lithium storage processes across all the potential regions at 90 °C.

To further ascertain the contribution of the capacitive mechanism(s) in the electrochemical performance of the Nb_2O_5 electrode at the different scan rates, Equation 3 and 4 shown below are applied.[62] It is worth noting that the current derived from diffusion (i_{diff}) varies with the square root of v, while the capacitive current (i_{cap}) shows a linear relationship with v.

$$i = i_{cap} + i_{diff}$$
$$= k_1 v + k_2 v^{1/2} \quad (3)$$
$$i/v^{1/2} = k_1/v^{1/2} + k_2 \quad (4)$$

The k_1 and k_2 are constants at each applied potential. The capacitive contribution in the charge storage process can therefore be determined by calculating the k_1 and k_2 values as shown in **Figure 4e,f**. For a clear visualisation, the CV profile for capacitive mechanism(s) derived from k_1 and k_2 values (shown by the bright orange region in the **Figure 4e** has been presented alongside the CV experimentally obtained at a scan rate of 5 mV s^{-1} for comparison. The voltammograms reveal the capacitive contribution to be 37% at 25 °C and 71% at 90 °C. The capacitive-derived currents (= i_{cap} / (i_{cap} + i_{diff})) obtained under various scan rates at 25 and 90 °C are further deconvoluted and summarized in **Figure 4f**. As shown in the graph, the capacitive contribution increased when the scan rates were increased. Additionally, the capacitive contribution was significantly higher at 90 °C than at 25 °C—attesting to the dominance of capacitive response and consequently the enhanced ion diffusion at elevated temperatures. It should be pointed out that the experimental CV

analysis investigating the capacitive contribution was restricted to scan rates in the 0.5–10 mV s^{-1} range to avoid ohmic polarization commonly observed in profiles at high rates.[63] These CV-based analyses on the capacitive behavior well-explain the different rate-capability trends at 25 and 90 °C. Accordingly, the contribution of the diffusion-controlled process to the overall capacity was seen to decrease at high rates and with increasing operating temperature, in proportion to the increases in the capacitive process.

Interfacial properties of a-$Li_xNb_2O_5$ and SEI formation. For insight into the effect of temperature on the interfacial behavior of the Nb_2O_5 electrode, SCEIS analysis was performed at varying temperatures. To eliminate the influence of the metal counter electrode (in this case Li metal) in the half-cell configuration, SCEIS is typically performed on a symmetric cell comprising two identical electrodes (in this case Nb_2O_5) at the same state of charge (SOC) to discern the charge transfer properties (impedance) of an electrode.[64, 65] As such, SCEIS was performed on symmetric cells (**Figure 5a**) at the SOC of 40% at temperatures of 25, 70 and 90 °C. The data obtained from the SCEIS tests were rendered into the equivalent circuit displayed in **Figure 5a**, where R_h represents the resistance in the high-frequency range, R_{ct} corresponds to the charge transfer resistance in the faradaic process(es), and C_{dl} shows the capacitance element for double-layer capacitance and CPE_{pseudo} is a constant phase element (CPE) for pseudocapacitance. The position of R_{ct} is designated based on the characteristic frequencies provided in **Table S3**.

Nyquist plots of the Nb_2O_5/IL/Nb_2O_5 cells were obtained over the 0.1 Hz–100 kHz frequency range, as shown in **Figure 5b**. To visualise the effect of temperature on the charge transfer resistance, the R_{ct} values from the EIS fitting results have been plotted in **Figure 5c**. The Nb_2O_5/IL/Nb_2O_5 cells exhibited a dramatic decrease in the R_{ct} resistance when operation temperatures were increased. These results confirm the beneficial role of temperature elevation in

the charge transfer mechanisms of the faradic redox reaction(s)—in agreement with the results from the rate performance tests.

On the equivalent circuit, R_{ct} is connected in series with the CPE_{pseudo} because its properties are derived from the redox process(es), whereas the C_{dl} is connected in parallel with the charge transfer component on the basis of its non-faradaic contribution. Therefore, it is possible to separate the pseudocapacitive process(es) from the double-layer capacitance process(es) in the equivalent circuit of the present EIS model.[66] The impedance (Z) of the CPE_{pseudo} can be derived using Equation 5 below;[67, 68]

$$Z_{CPE} = [B(j\omega)^n]^{-1} \qquad (5)$$

Here, B and n are frequency-independent adjustable constants, where j is the imaginary unit and ω is the angular frequency. The value of n = 0, 0.5, and 1 corresponds to the pure resistance, Warburg diffusion and ideal capacitance, respectively [69]. The values of n for CPE_{pseudo} in the present fitting are determined to be between 0.6 and 0.7 (See **Table S3**). As shown in **Figure 5d**, pseudocapacitance was observed to be temperature-dependent, with a dominant contribution to the total capacitance at 90 °C. However, the temperature variation is seen to have no significant effect on the contribution of the double-layer capacitance in the total capacitance. These results underpin the role of pseudocapacitive mechanism(s) in facilitating the fast kinetic behavior and the enhanced charge storage exhibited by the amorphous $Li_xNb_2O_5$ phase during intermediate temperature operations: in character with the results from the CV analyses.

In general, the quality of the SEI formed on an electrode is known to be the determining factor of battery cycle performance. As such, amorphous Nb_2O_5 electrodes (obtained after the 2nd charge) were subjected to further XPS analyses to understand the characteristics of the SEI layer

formed by the IL electrolyte at 25 and 90 °C. The STEM images show morphological evidence of existence of SEI formation after cycling with the cut-off voltage of 0.01–2.3 V (Figure S10). **Figure 6** shows the F 1s, C 1s, N 1s and S $2p_{3/2}$ XPS spectra of the Nb_2O_5 electrodes after the 2nd charge (see **Table S4** for peak assignments of the XPS). Here, the XPS spectra reveal an abundance of $[FSA]^-$-based SEI components (LiF: 684.5 eV and S-F: 687.6 eV in the F 1s spectrum, SO_x: 166 eV in the S $2p_{3/2}$ spectrum, and N-S 400.9 eV in the N 1s spectrum) on the surface of the Nb_2O_5 electrode regardless of the operating temperatures. It is worth noting that the amount of S- and N-based components are considered to be one of the key differentiators between SEI layers formed by organic electrolytes (*e.g.* Li[PF_6]-EC/DMC) and ionic liquid electrolytes (*e.g.* Li[FSA]-[C_2C_1im][FSA]). In fact, previous studies on NIBs and LIBs utilizing $[FSA]^-$-based electrolytes have identified the abundance of sulfur-based components in the SEI layer as the main factor behind their improved electrochemical performance in ILs.[70]

CONCLUSIONS

Herein, the influence of temperature on the pseudocapacitive behavior of Nb_2O_5 negative electrode was investigated in a wide cutoff voltage range of 0.01–2.3 V at 25 and 90 °C with the aid of a thermally stable Li[FSA]-[C_2C_1im][FSA] IL electrolyte. The structural evolution of the electrode after charge-discharge in the wide potential window was examined using *ex-situ* XRD (X-ray diffraction) and X-ray photoelectron spectroscopic (XPS) analyses. During the initial charge, the orthorhombic Nb_2O_5 undergo a transformation from the crystalline phase to an amorphous Nb_2O_5 accompanied by the formation of NbO via a conversion reaction. In the subsequent cycles, ultra-fast Li-storage processes ascribed to reversible $Nb^{V,IV}/Nb^{III}$ redox reactions were observed in the amorphous $Li_xNb_2O_5$. At 90 °C, the electrode exhibited a high-rate capability (up to 20000 mA g^{-1}) and long-term cycle life (over 2000 cycles at 2000 mA g^{-1}) with an average Coulombic

efficiency of 99.4%. The auspicious role of temperature elevation in the performance of the pseudocapacitive properties electrode is particularly highlighted by the short discharge time of around 20 seconds (20000 mA g^{-1}) and the high-capacity retention. The pseudocapacitive effect of the Nb_2O_5 was also quantitatively determined through *b*-value analysis on data derived from CV and SCEIS evaluations. The pseudocapacitive effect of Nb_2O_5 was noted to have a higher contribution to the total capacity of the electrode when the rate was increased and at higher temperatures. The enhanced performance of the Nb_2O_5 electrode was attributed to the formation of an $[FSA]^-$ originated SEI layer during the initial charge, earmarking the vital role of the IL electrolyte in the exploration of advanced energy systems.

This study linked the operating temperature and pseudocapacitive behavior of Nb_2O_5, consequently offering an efficient way to enhance electrochemical properties and revealing the capacitive processes of Nb_2O_5 and lithium storage mechanism including the phase transition. It is also an attractive means of circumventing complex structures or surface engineering to approach a practical application on advanced electrochemical energy storage devices.

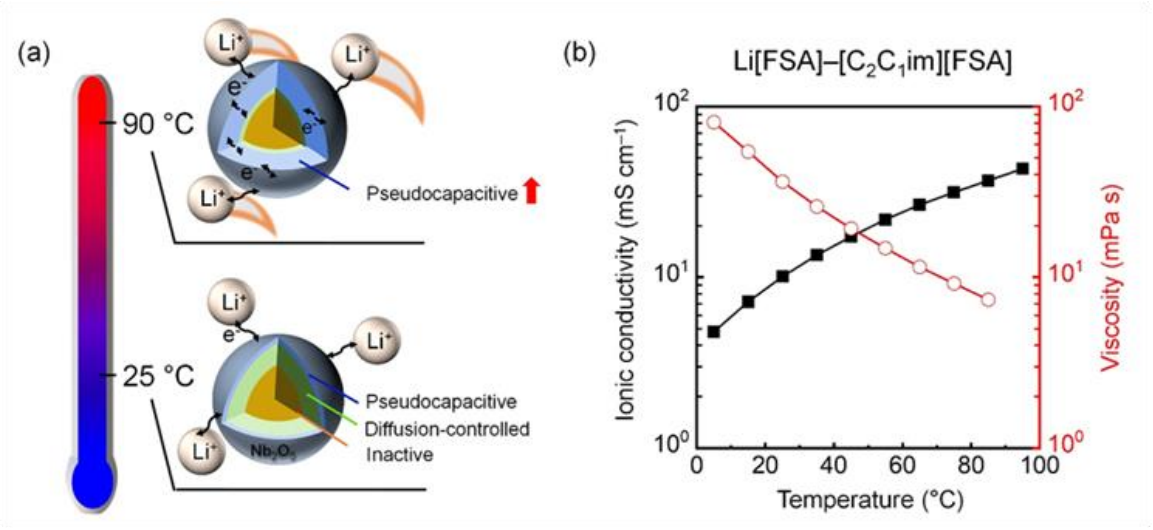

Figure 1. (a) Schematic illustration of the effect of temperature on the pseudocapacitive contribution in the Li storage mechanisms of submicron-sized Nb_2O_5 energy material. (b) The correlation between temperature elevation and ionic conductivity and viscosity of the Li[FSA]-[C_2C_1im][FSA] (20:80 in mol) IL electrolyte.[46] Reprinted with permission.[46] Copyright 2017 American Chemical Society.

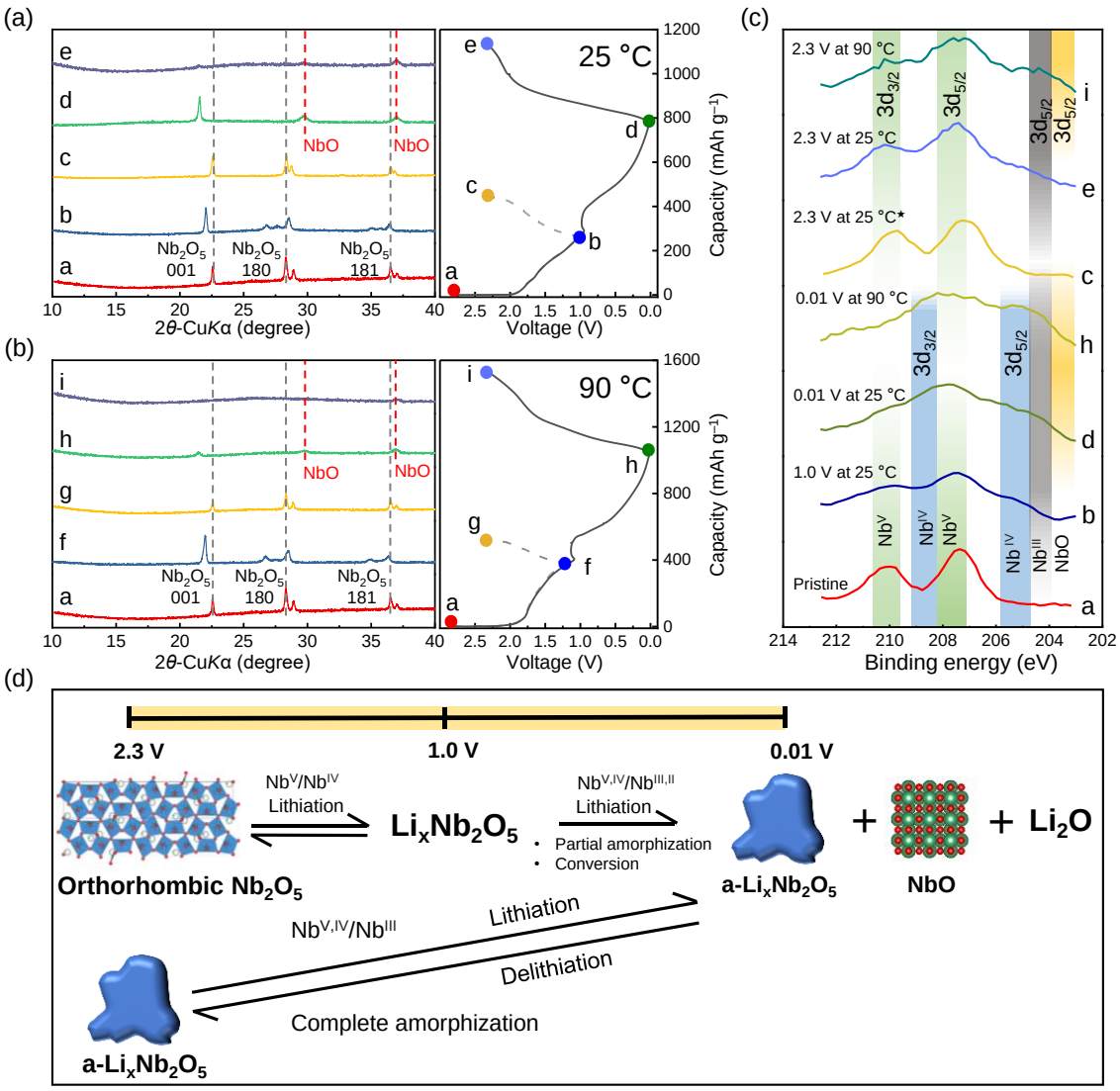

Figure 2. (a, b) Ex-situ XRD patterns at various SOCs of the Nb_2O_5 in the Li[FSA]-[C_2C_1im][FSA] IL at (a) 25 and (b) 90 °C. Dashed lines of the orthorhombic Nb_2O_5 and cubic NbO are drawn from the previous data of JCPDS 01-071-0336 for Nb_2O_5 and JCPDS 01-071-2146 for NbO, respectively.[55,58] See **Figures S2** and **S4** for reference patterns of Nb_2O_5 and NbO, respectively. (c) *Ex-situ* XPS spectra of the pristine and (de)lithiated Nb_2O_5 in the Li[FSA]-[C_2C_1im][FSA] IL at 25 and 90 °C. The ★ mark is used to denote the discharged sample from 1.0 to 2.3 V (charge-discharge curve point c) at 25 °C. (d) Schematic illustration of the charge-discharge mechanism of the orthorhombic-Nb_2O_5 (a-$Li_xNb_2O_5$ after the initial cycle).

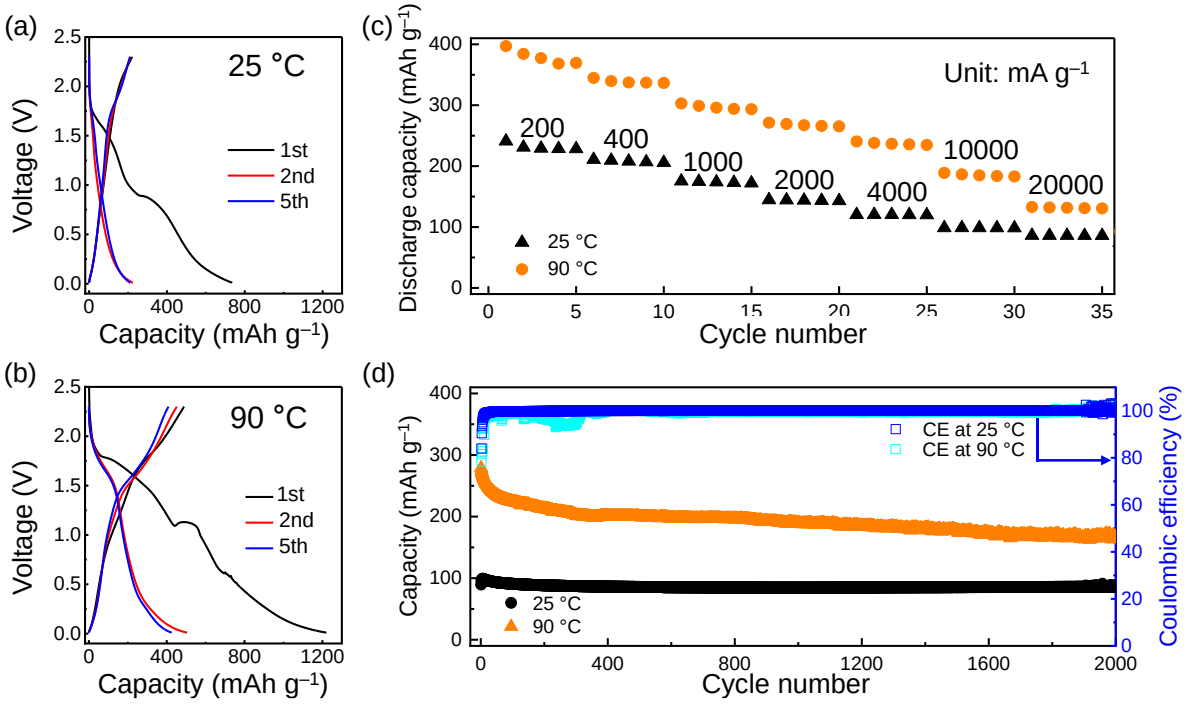

Figure 3. Electrochemical performance of the Li/IL/Nb_2O_5 cells (IL = Li[FSA]-[C_2C_1im][FSA] (20:80 in mol)). Charge-discharge curves in the 0.01–2.3 V cutoff voltage range and current density of 200 mA g^{-1} at (a) 25 and (b) 90 °C. (c) Rate capability at 25 and 90 °C. The current density for charge: 200 mA g^{-1}. The current density for discharge: 200–20000 mA g^{-1}. Cutoff voltage: 0.01–2.3 V. See **Figure S5** and **Table S1** for the corresponding discharge curves and details on the capacity, capacity retention, and geometric current density of rate capability, respectively. (d) Cycle performance at 25 and 90 °C. Current densities for both charge and discharge: 2000 mA g^{-1} and cutoff voltage: 0.01–2.3 V. See **Figure S6** and **Table S2** for the corresponding charge-discharge curves and details of capacity and capacity retention during cycle performance, respectively.

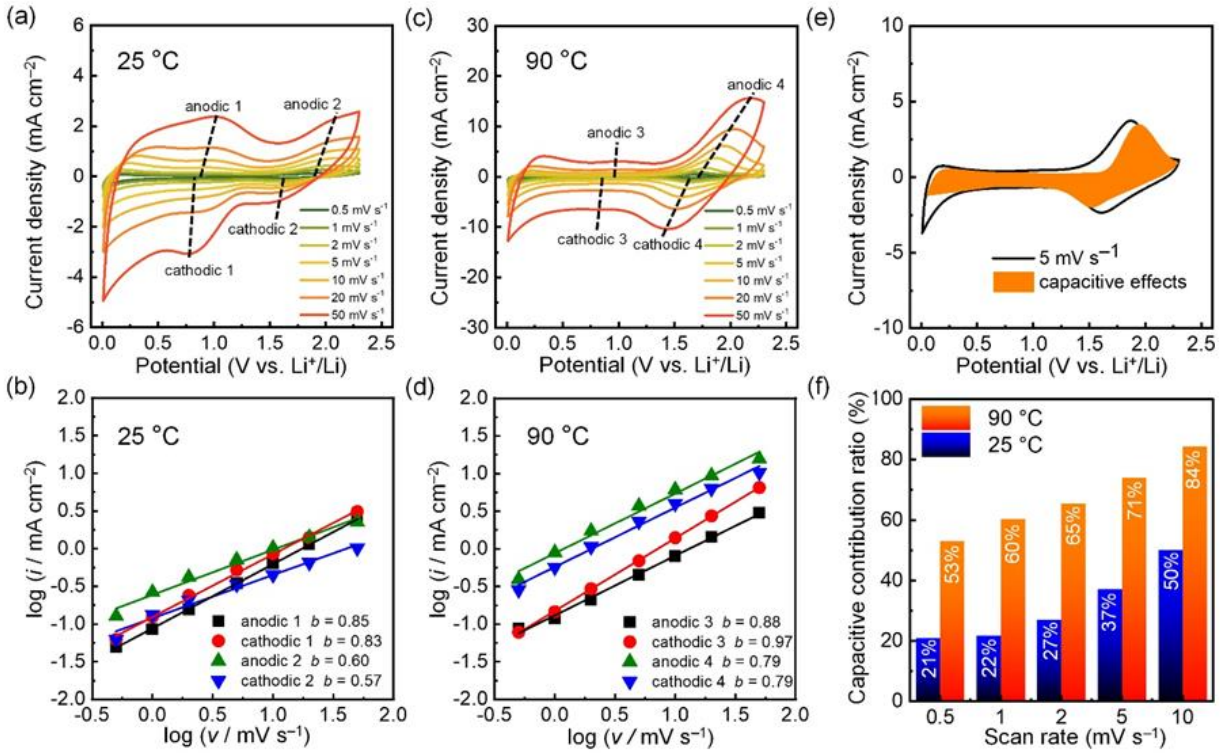

Figure 4. Kinetic analysis of the electrochemical performance of Nb_2O_5 electrodes in the Li/IL/Nb_2O_5 cells at 25 and 90 °C (IL = Li[FSA]-[C_2C_1im][FSA] (20:80 in mol). Cyclic voltammograms at scan rates from 0.5 to 50 mV s^{-1} at (a) 25 and (c) 90 °C (3rd cycle of each scan rate is plotted). (b, d) The log(*i*)-log(*v*) plot for *b*-value determination of cathodic and anodic peaks at (b) 25 and (d) 90 °C. (e) Voltametric responses at a scan rate of 5 mV s^{-1} at 90 °C. The bright orange region represents the capacitive responses derived from k_1 and k_2 analysis. (f) Comparison of capacitive contribution of capacitive current at 25 and 90 °C at different scan rates.

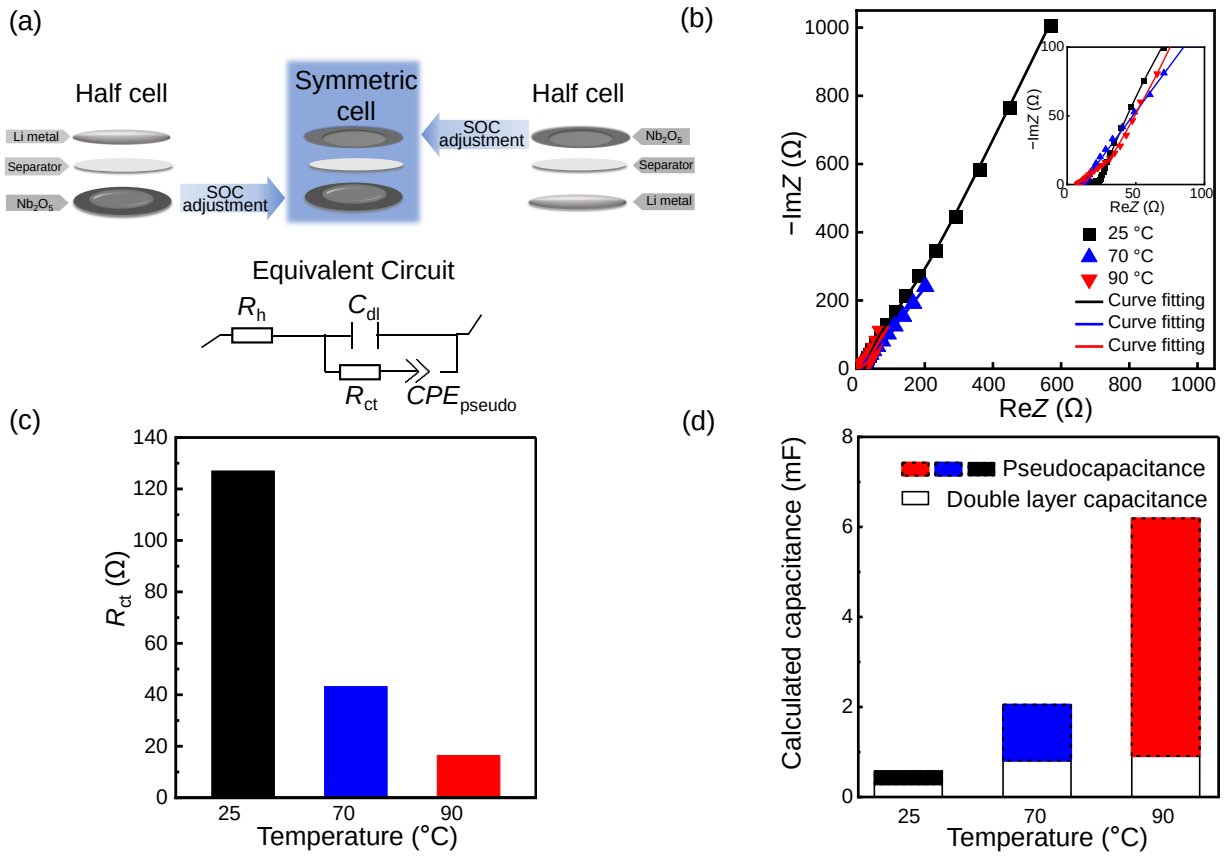

Figure 5. Analysis for the effect of temperature on the electrochemical behavior of the Nb_2O_5 through SCEIS on a Nb_2O_5/IL/Nb_2O_5 symmetric cell. IL = Li[FSA]-[C_2C_1im][FSA] (20:80 in mol) IL electrolyte. (a) Schematic illustration of the preparation of symmetric cell using two SOC-adjusted Nb_2O_5 electrodes and an equivalent circuit to fit the Nyquist plots. (b) Nyquist plots of the Nb_2O_5/IL/Nb_2O_5 symmetric cells at SOCs of 1.0 V at 25, 70 and 90 °C. Frequency range: 0.1 Hz–100 kHz. The high-frequency region of (b) is shown in the inset. (c, d) Dependence of (c) R_{ct} and (d) capacitance upon applied temperatures for the Nb_2O_5 electrodes at 25, 70 and 90 °C, respectively. (See **Table S3** for the EIS fitting results).

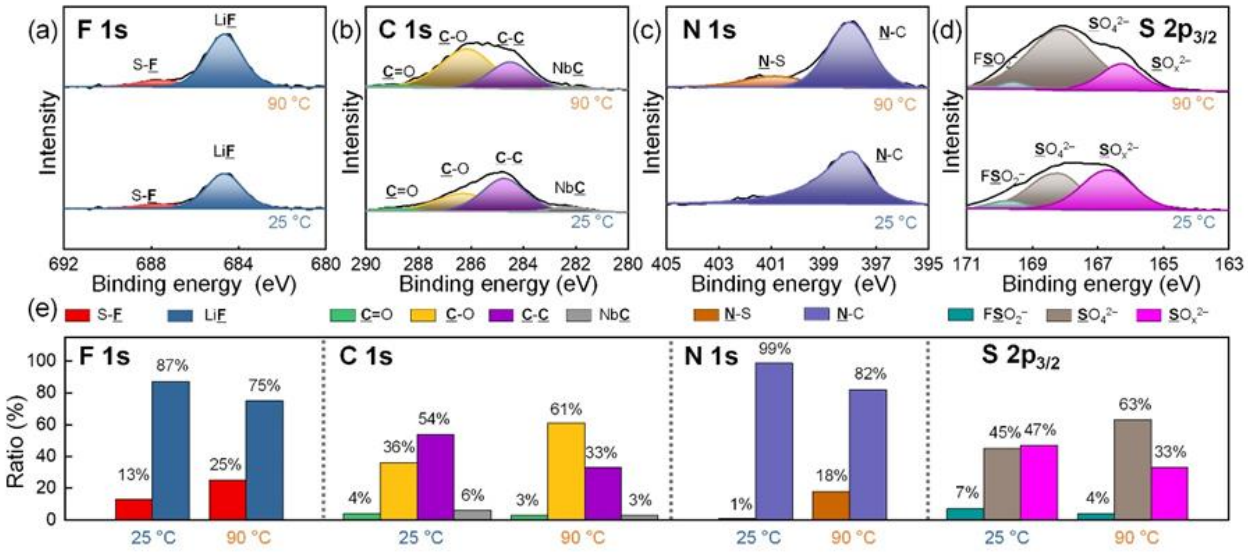

Figure 6. XPS analysis of the SEI layers formed on Nb_2O_5 in the Li[FSA]-[C_2C_1im][FSA] IL after 2nd charge at 25 and 90 °C. (a) F 1s, (b) C 1s, (c) N 1s and (d) S $2p_{3/2}$ regions, and (e) SEI component ratios (See **Table S4** for the fitting results).

ASSOCIATED CONTENT

Supporting Information.

The Supporting Information is available free of charge at DOI: xx.

XRD, BET surface area, additional electrochemical properties with additional discussion, and SEI composition data (PDF)

AUTHOR INFORMATION

Corresponding Author

*Phone: +81 75 753 5827. Fax: +81 75 753 5906.

E-mail: hwang.jinkwang.5c@kyoto-u.ac.jp and k-matsumoto@energy.kyoto-u.ac.jp

ORCID

Shaoning. Zhang: 0000-0003-1727-5863

Jinkwang Hwang: 0000-0003-4800-3158

Kazuhiko Matsumoto: 0000-0002-0770-9210

Rika Hagiwara: 0000-0002-7234-3980

Notes

The authors declare no competing financial interest.

ACKNOWLEDGMENT

This study was supported by the Japan Society for the Promotion of Science (JSPS, KAKENHI Grant Number 19H02811).

REFERENCES

(1) Dunn, B.; Kamath, H.; Tarascon, J.-M. Electrical Energy Storage for the Grid: A Battery of Choices. *Science* **2011,** *334*, 928-935.

(2) Marom, R.; Amalraj, S. F.; Leifer, N.; Jacob, D.; Aurbach, D. A review of advanced and practical lithium battery materials. *J. Mater. Chem.* **2011,** *21*, 9938-9954.

(3) Amine, K.; Belharouak, I.; Chen, Z.; Tran, T.; Yumoto, H.; Ota, N.; Myung, S.-T.; Sun, Y.-K. Nanostructured Anode Material for High-Power Battery System in Electric Vehicles. *Adv. Mater.* **2010,** *22*, 3052-3057.

(4) Liu, A.; Zhang, H.; Xing, C.; Wang, Y.; Zhang, J.; Zhang, X.; Zhang, S. Intensified Energy Storage in High-Voltage Nanohybrid Supercapacitors via the Efficient Coupling between $TiNb_2O_7$/Holey-rGO Nanoarchitectures and Ionic Liquid-Based Electrolytes. *ACS Appl. Mater. Interfaces* **2021,** *13*, 21349-21361.

(5) Maletti, S.; Janson, O.; Herzog-Arbeitman, A.; Gonzalez Martinez, I. G.; Buckan, R.; Fischer, J.; Senyshyn, A.; Missyul, A.; Etter, M.; Mikhailova, D. Operation Mechanism in Hybrid Mg–Li Batteries with $TiNb_2O_7$ Allowing Stable High-Rate Cycling. *ACS Appl. Mater. Interfaces* **2021,** *13*, 6309-6321.

(6) Meng, X.; Xu, Y.; Cao, H.; Lin, X.; Ning, P.; Zhang, Y.; Garcia, Y. G.; Sun, Z. Internal failure of anode materials for lithium batteries — A critical review. *Green Energy Environ.* **2020,** *5*, 22-36.

(7) Liu, Y.; Zhu, Y.; Cui, Y. Challenges and opportunities towards fast-charging battery materials. *Nature Energy* **2019,** *4*, 540-550.

(8) Magasinski, A.; Dixon, P.; Hertzberg, B.; Kvit, A.; Ayala, J.; Yushin, G. High-performance lithium-ion anodes using a hierarchical bottom-up approach. *Nat. Mater.* **2010,** *9*, 353-358.

(9) Eshetu, G. G.; Zhang, H.; Judez, X.; Adenusi, H.; Armand, M.; Passerini, S.; Figgemeier, E. Production of high-energy Li-ion batteries comprising silicon-containing anodes and insertion-type cathodes. *Nat. Commun.* **2021,** *12,* 5459.

(10) Shin, H.-J.; Hwang, J.-Y.; Kwon, H. J.; Kwak, W.-J.; Kim, S.-O.; Kim, H.-S.; Jung, H.-G. Sustainable Encapsulation Strategy of Silicon Nanoparticles in Microcarbon Sphere for High-Performance Lithium-Ion Battery Anode. *ACS Sustain. Chem. Eng.* **2020,** *8,* 14150-14158.

(11) Yuan, T.; Tan, Z.; Ma, C.; Yang, J.; Ma, Z.-F.; Zheng, S. Challenges of Spinel $Li_4Ti_5O_{12}$ for Lithium-Ion Battery Industrial Applications. *Adv. Energy Mater.* **2017,** *7,* 1601625.

(12) Han, C.; He, Y.-B.; Liu, M.; Li, B.; Yang, Q.-H.; Wong, C.-P.; Kang, F. A review of gassing behavior in $Li_4Ti_5O_{12}$-based lithium ion batteries. *J. Mater. Chem. A* **2017,** *5,* 6368-6381.

(13) Deng, Q.; Fu, Y.; Zhu, C.; Yu, Y. Niobium-Based Oxides Toward Advanced Electrochemical Energy Storage: Recent Advances and Challenges. *Small* **2019,** *15,* 1804884.

(14) Sun, H.; Mei, L.; Liang, J.; Zhao, Z.; Lee, C.; Fei, H.; Ding, M.; Lau, J.; Li, M.; Wang, C.; et al. Three-dimensional holey-graphene/niobia composite architectures for ultrahigh-rate energy storage. *Science* **2017,** *356,* 599-604.

(15) Kim, J. W.; Augustyn, V.; Dunn, B. The Effect of Crystallinity on the Rapid Pseudocapacitive Response of Nb_2O_5. *Adv. Energy Mater.* **2012,** *2,* 141-148.

(16) Sathasivam, S.; Williamson, B. A. D.; Althabaiti, S. A.; Obaid, A. Y.; Basahel, S. N.; Mokhtar, M.; Scanlon, D. O.; Carmalt, C. J.; Parkin, I. P. Chemical Vapor Deposition Synthesis and Optical Properties of Nb_2O_5 Thin Films with Hybrid Functional Theoretical Insight into the Band Structure and Band Gaps. *ACS Appl. Mater. Interfaces* **2017,** *9,* 18031-18038.

(17) Yang, M.; Li, S.; Huang, J. Three-Dimensional Cross-Linked Nb_2O_5 Polymorphs Derived from Cellulose Substances: Insights into the Mechanisms of Lithium Storage. *ACS Appl. Mater. Interfaces* **2021,** *13,* 39501-39512.

(18) Griffith, K. J.; Forse, A. C.; Griffin, J. M.; Grey, C. P. High-Rate Intercalation without Nanostructuring in Metastable Nb_2O_5 Bronze Phases. *J. Am. Chem. Soc.* **2016,** *138,* 8888-8899.

(19) Augustyn, V.; Come, J.; Lowe, M. A.; Kim, J. W.; Taberna, P.-L.; Tolbert, S. H.; Abruña, H. D.; Simon, P.; Dunn, B. High-rate electrochemical energy storage through Li^+ intercalation pseudocapacitance. *Nat. Mater.* **2013,** *12,* 518-522.

(20) Chen, D.; Wang, J.-H.; Chou, T.-F.; Zhao, B.; El-Sayed, M. A.; Liu, M. Unraveling the Nature of Anomalously Fast Energy Storage in T-Nb_2O_5. *J. Am. Chem. Soc.* **2017,** *139,* 7071-7081.

(21) Fleischmann, S.; Mitchell, J. B.; Wang, R.; Zhan, C.; Jiang, D.-e.; Presser, V.; Augustyn, V. Pseudocapacitance: From Fundamental Understanding to High Power Energy Storage Materials. *Chemical Reviews* **2020,** *120,* 6738-6782.

(22) Cook, J. B.; Detsi, E.; Liu, Y.; Liang, Y.-L.; Kim, H.-S.; Petrissans, X.; Dunn, B.; Tolbert, S. H. Nanoporous Tin with a Granular Hierarchical Ligament Morphology as a Highly Stable Li-Ion Battery Anode. *ACS Appl. Mater. Interfaces* **2017,** *9,* 293-303.

(23) Song, M. Y.; Kim, N. R.; Yoon, H. J.; Cho, S. Y.; Jin, H.-J.; Yun, Y. S. Long-Lasting Nb_2O_5-Based Nanocomposite Materials for Li-Ion Storage. *ACS Appl. Mater. Interfaces* **2017,** *9,* 2267-2274.

(24) Zhang, M.; He, Y.-X.; Xu, H.-J.; Ma, C.; Liang, J.-F.; Wang, Y.-Y.; Zhu, J. Nb_2O_5 nanoparticles embedding in graphite hybrid as a high-rate and long-cycle anode for lithium-ion batteries. *Rare Met.* **2022,** *41,* 814-821.

(25) Liu, M.; Yan, C.; Zhang, Y. Fabrication of Nb_2O_5 Nanosheets for High-rate Lithium Ion Storage Applications. *Sci. Rep.* **2015,** *5*, 8326.

(26) Kim, H.-S.; Cook, J. B.; Lin, H.; Ko, Jesse S.; Tolbert, Sarah H.; Ozolins, V.; Dunn, B. Oxygen vacancies enhance pseudocapacitive charge storage properties of MoO_{3-x}. *Nat. Mater.* **2017,** *16*, 454-460.

(27) Li, N.; Lan, X.; Wang, L.; Jiang, Y.; Guo, S.; Li, Y.; Hu, X. Precisely Tunable *T*-Nb_2O_5 Nanotubes via Atomic Layer Deposition for Fast-Charging Lithium-Ion Batteries. *ACS Appl. Mater. Interfaces* **2021,** *13*, 16445-16453.

(28) Kong, L.; Liu, X.; Wei, J.; Wang, S.; Xu, B. B.; Long, D.; Chen, F. *T*-Nb_2O_5 nanoparticle enabled pseudocapacitance with fast Li-ion intercalation. *Nanoscale* **2018,** *10*, 14165-14170.

(29) Cook, J. B.; Lin, T. C.; Kim, H.-S.; Siordia, A.; Dunn, B. S.; Tolbert, S. H. Suppression of Electrochemically Driven Phase Transitions in Nanostructured MoS_2 Pseudocapacitors Probed Using Operando X-ray Diffraction. *ACS Nano* **2019,** *13*, 1223-1231.

(30) Zhao, H.; Qi, Y.; Liang, K.; Li, J.; Zhou, L.; Chen, J.; Huang, X.; Ren, Y. Interface-Driven Pseudocapacitance Endowing Sandwiched $CoSe_2$/N-Doped Carbon/TiO_2 Microcubes with Ultra-Stable Sodium Storage and Long-Term Cycling Stability. *ACS Appl. Mater. Interfaces* **2021,** *13*, 61555-61564.

(31) Wagemaker, M.; Mulder, F. M. Properties and Promises of Nanosized Insertion Materials for Li-Ion Batteries. *Acc. Chem. Res.* **2013,** *46*, 1206-1215.

(32) Sudant, G.; Baudrin, E.; Larcher, D.; Tarascon, J.-M. Electrochemical lithium reactivity with nanotextured anatase-type TiO_2. *J. Mater. Chem.* **2005,** *15*, 1263-1269.

(33) Hwang, J.; Matsumoto, K.; Hagiwara, R. Electrolytes toward High-Voltage $Na_3V_2(PO_4)_2F_3$ Positive Electrode Durable against Temperature Variation. *Adv. Energy Mater.* **2020,** *10*, 2001880.

(34) Xu, K. Nonaqueous Liquid Electrolytes for Lithium-Based Rechargeable Batteries. *Chem. Rev.* **2004,** *104*, 4303-4418.

(35) Hess, S.; Wohlfahrt-Mehrens, M.; Wachtler, M. Flammability of Li-Ion Battery Electrolytes: Flash Point and Self-Extinguishing Time Measurements. *J. Electrochem. Soc.* **2015,** *162*, A3084-A3097.

(36) Cabrera-Castillo, E.; Niedermeier, F.; Jossen, A. Calculation of the state of safety (SOS) for lithium ion batteries. *J. Power Sources* **2016,** *324*, 509-520.

(37) Hwang, J.; Matsumoto, K.; Chen, C.-Y.; Hagiwara, R. Pseudo-solid-state electrolytes utilizing the ionic liquid family for rechargeable batteries. *Energy Environ. Sci.* **2021,** *14*, 5834-5863.

(38) Watanabe, M.; Thomas, M. L.; Zhang, S.; Ueno, K.; Yasuda, T.; Dokko, K. Application of Ionic Liquids to Energy Storage and Conversion Materials and Devices. *Chem. Rev.* **2017,** *117*, 7190-7239.

(39) Hwang, J.; Okada, H.; Haraguchi, R.; Tawa, S.; Matsumoto, K.; Hagiwara, R. Ionic liquid electrolyte for room to intermediate temperature operating Li metal batteries: Dendrite suppression and improved performance. *J. Power Sources* **2020,** *453*, 227911.

(40) Wang, D.; Hwang, J.; Chen, C.-y.; Kubota, K.; Matsumoto, K.; Hagiwara, R. A *β*”-Alumina/Inorganic Ionic Liquid Dual Electrolyte for Intermediate-Temperature Sodium–Sulfur Batteries. *Adv. Funct. Mater.* **2021,** *31*, 2105524.

(41) Lübke, M.; Sumboja, A.; Johnson, I. D.; Brett, D. J. L.; Shearing, P. R.; Liu, Z.; Darr, J. A. High power nano-Nb_2O_5 negative electrodes for lithium-ion batteries. *Electrochim. Acta* **2016,** *192*, 363-369.

(42) Lin, J.; Yuan, Y.; Su, Q.; Pan, A.; Dinesh, S.; Peng, C.; Cao, G.; Liang, S. Facile synthesis of Nb_2O_5/carbon nanocomposites as advanced anode materials for lithium-ion batteries. *Electrochim. Acta* **2018,** *292*, 63-71.

(43) Qu, X.; Liu, Y.; Li, B.; Xing, B.; Huang, G.; Zhang, C.; Hong, S. W.; Yu, J.; Cao, Y. Synthesis of High Reversibility Anode Composite Materials Using *T*-Nb_2O_5 and Coal-Based Graphite for Lithium-Ion Battery Applications. *Energy Fuels* **2020,** *34*, 3887-3894.

(44) Zhu, S.; Xu, P.; Liu, J.; Sun, J. Atomic layer deposition and structure optimization of ultrathin Nb_2O_5 films on carbon nanotubes for high-rate and long-life lithium ion storage. *Electrochim. Acta* **2020,** *331*, 135268.

(45) Kim, H.; Lim, E.; Jo, C.; Yoon, G.; Hwang, J.; Jeong, S.; Lee, J.; Kang, K. Ordered-mesoporous Nb_2O_5/carbon composite as a sodium insertion material. *Nano Energy* **2015,** *16*, 62-70.

(46) Matsumoto, K.; Nishiwaki, E.; Hosokawa, T.; Tawa, S.; Nohira, T.; Hagiwara, R. Thermal, Physical, and Electrochemical Properties of $Li[N(SO_2F)_2]$-[1-Ethyl-3-methylimidazolium][$N(SO_2F)_2$] Ionic Liquid Electrolytes for Li Secondary Batteries Operated at Room and Intermediate Temperatures. *J. Phys. Chem. C* **2017,** *121*, 9209-9219.

(47) Momma, K.; Izumi, F. VESTA: a three-dimensional visualization system for electronic and structural analysis. *J. Appl. Crystallogr.* **2008,** *41*, 653-658.

(48) Hwang, J.; Matsumoto, K.; Orikasa, Y.; Katayama, M.; Inada, Y.; Nohira, T.; Hagiwara, R. Crystalline maricite $NaFePO_4$ as a positive electrode material for sodium secondary batteries operating at intermediate temperature. *J. Power Sources* **2018,** *377*, 80-86.

(49) Li, S.; Xu, Q.; Uchaker, E.; Cao, X.; Cao, G. Comparison of amorphous, pseudohexagonal and orthorhombic Nb_2O_5 for high-rate lithium ion insertion. *CrystEngComm* **2016,** *18*, 2532-2540.

(50) Lian, Y.; Wang, D.; Hou, S.; Ban, C.; Zhao, J.; Zhang, H. Construction of *T*-Nb_2O_5 nanoparticles on/in N-doped carbon hollow tubes for Li-ion hybrid supercapacitors. *Electrochim. Acta* **2020,** *330*, 135204.

(51) Yang, K.; Peng, J.; Srinivasakannan, C.; Zhang, L.; Xia, H.; Duan, X. Preparation of high surface area activated carbon from coconut shells using microwave heating. *Bioresour. Technol.* **2010,** *101*, 6163-6169.

(52) Choudhury, T.; Saied, S. O.; Sullivan, J. L.; Abbot, A. M. Reduction of oxides of iron, cobalt, titanium and niobium by low-energy ion bombardment. *J. Phys. D Appl. Phys.* **1989,** *22*, 1185-1195.

(53) McGuire, G. E.; Schweitzer, G. K.; Carlson, T. A. Core electron binding energies in some Group IIIA, VB, and VIB compounds. *Inorg. Chem.* **1973,** *12*, 2450-2453.

(54) Jung, K.; Kim, Y.; Park, Y. S.; Jung, W.; Choi, J.; Park, B.; Kim, H.; Kim, W.; Hong, J.; Im, H. Unipolar resistive switching in insulating niobium oxide film and probing electroforming induced metallic components. *J. Appl. Phys.* **2011,** *109*.

(55) Kato, K.; Tamura, S. Die Kristallstruktur von T-Nb_2O_5. *Acta Crystallogr., Sect. B: Struct. Sci., Cryst. Eng. Mater.* **1975,** *31*, 673-677.

(56) Atuchin, V. V.; Kalabin, I. E.; Kesler, V. G.; Pervukhina, N. V. Nb 3d and O 1s core levels and chemical bonding in niobates. *J. Electron. Spectrosc. Relat. Phenom.* **2005,** *142*, 129-134.

(57) Come, J.; Augustyn, V.; Kim, J. W.; Rozier, P.; Taberna, P.-L.; Gogotsi, P.; Long, J. W.; Dunn, B.; Simon, P. Electrochemical Kinetics of Nanostructured Nb_2O_5 Electrodes. *J. Electrochem. Soc.* **2014,** *161*, A718-A725.

(58) Bowman, A. L.; Wallace, T. C.; Yarnell, J. L.; Wenzel, R. G. The crystal structure of niobium monoxide. *Acta Crystallogr.* **1966,** *21*, 843.

(59) Chae, O. B.; Kim, J.; Park, I.; Jeong, H.; Ku, J. H.; Ryu, J. H.; Kang, K.; Oh, S. M. Reversible Lithium Storage at Highly Populated Vacant Sites in an Amorphous Vanadium Pentoxide Electrode. *Chem. Mater.* **2014,** *26*, 5874-5881.

(60) Yu, Z.; Zhu, G.; Xu, H.; Yu, A. Amorphous $Li_4Ti_5O_{12}$ Thin Film with Enhanced Lithium Storage Capability and Reversibility for Lithium-Ion Batteries. *Energy Technol.* **2014,** *2*, 767-772.

(61) Lindström, H.; Södergren, S.; Solbrand, A.; Rensmo, H.; Hjelm, J.; Hagfeldt, A.; Lindquist, S.-E. Li^+ Ion Insertion in TiO_2 (Anatase). 2. Voltammetry on Nanoporous Films. *J. Phys. Chem. B* **1997,** *101*, 7717-7722.

(62) Liu, T. C.; Pell, W. G.; Conway, B. E.; Roberson, S. L. Behavior of Molybdenum Nitrides as Materials for Electrochemical Capacitors: Comparison with Ruthenium Oxide. *J. Electrochem. Soc.* **1998,** *145*, 1882-1888.

(63) Pu, X.; Zhao, D.; Fu, C.; Chen, Z.; Cao, S.; Wang, C.; Cao, Y. Understanding and Calibration of Charge Storage Mechanism in Cyclic Voltammetry Curves. *Angew. Chem. Int. Ed.* **2021,** *60*, 21310-21318.

(64) Hwang, J.; Matsumoto, K.; Hagiwara, R. Symmetric Cell Electrochemical Impedance Spectroscopy of $Na_2FeP_2O_7$ Positive Electrode Material in Ionic Liquid Electrolytes. *J. Phys. Chem. C* **2018,** *122*, 26857-26864.

(65) Ogihara, N.; Kawauchi, S.; Okuda, C.; Itou, Y.; Takeuchi, Y.; Ukyo, Y. Theoretical and Experimental Analysis of Porous Electrodes for Lithium-Ion Batteries by Electrochemical Impedance Spectroscopy Using a Symmetric Cell. *J. Electrochem. Soc.* **2012,** *159*, A1034-A1039.

(66) Brezesinski, T.; Wang, J.; Senter, R.; Brezesinski, K.; Dunn, B.; Tolbert, S. H. On the Correlation between Mechanical Flexibility, Nanoscale Structure, and Charge Storage in Periodic Mesoporous CeO_2 Thin Films. *ACS Nano* **2010,** *4*, 967-977.

(67) Sugimoto, W.; Iwata, H.; Yokoshima, K.; Murakami, Y.; Takasu, Y. Proton and Electron Conductivity in Hydrous Ruthenium Oxides Evaluated by Electrochemical Impedance Spectroscopy: The Origin of Large Capacitance. *J. Phys. Chem. B* **2005,** *109,* 7330-7338.

(68) Nilson, R. H.; Brumbach, M. T.; Bunker, B. C. Modeling the Electrochemical Impedance Spectra of Electroactive Pseudocapacitor Materials. *J. Electrochem. Soc.* **2011,** *158,* A678.

(69) Miller, J. M.; Dunn, B. Morphology and Electrochemistry of Ruthenium/Carbon Aerogel Nanostructures. *Langmuir* **1999,** *15,* 799-806.

(70) Kaushik, S.; Matsumoto, K.; Hagiwara, R. Stable Cycle Performance of a Phosphorus Negative Electrode in Lithium-Ion Batteries Derived from Ionic Liquid Electrolytes. *ACS Appl. Mater. Interfaces* **2021,** *13,* 10891-10901.

TOC GRAPHICS